Nonlinear nano-imaging of interlayer coupling in 2D graphene-semiconductor heterostructures

Wenjin Luo, *Renkang Song*, *Benjamin G. Whetten*, *Di Huang*, *Xinbin Cheng*, *Alexey Belyanin**, *Tao Jiang** and *Markus B. Raschke**

W. Luo, R. Song, D. Huang, X. Cheng, T. Jiang

MOE Key Laboratory of Advanced Micro-Structured Materials, Shanghai Frontiers Science Center of Digital Optics, Institute of Precision Optical Engineering, and School of Physics Science and Engineering, Tongji University, Shanghai 200092, China

Email Address: tjiang@tongji.edu.cn

W. Luo, B. G. Whetten, M. B. Raschke

Department of Physics and JILA, University of Colorado, Boulder, CO 80309, USA

Email Address: markus.raschke@colorado.edu

A. Belyanin

Department of Physics and Astronomy, Texas A&M University, College Station, Texas 77843, USA

Email Address: belyanin@physics.tamu.edu

Keywords: *interlayer coupling, 2D heterostructure, energy transfer, nonlinear optics, FWM/2PPL nanoimaging*

Two-dimensional heterostructures of graphene and transition metal dichalcogenides exhibit enhanced photonic, electronic, spin, and other novel quantum properties. These emergent phenomena are controlled by the underlying interlayer coupling and associated charge and energy transfer and their dynamics. However, these processes are sensitive to interlayer distance and relative crystallographic orientation, which are in turn affected by defects, grain boundaries, bubbles, local strain, and other nanoscale heterogeneities. This obfuscates the distinction between interlayer charge and energy transfer and their competition with other relaxation processes, further amplified by spatial averaging across sample heterogeneities in conventional spectroscopy techniques. Here we combine nanoscale imaging in coherent four-wave mixing (FWM) and incoherent two-photon photoluminescence (2PPL) with a tip distance-dependent coupled rate equation model to resolve the underlying intra- and inter-layer dynamics while avoiding the influence of structural heterogeneities in mono- to multi-layer graphene/WSe_2 heterostructures. With selective insertion of hBN spacer layers, we show that energy as opposed to charge transfer dominates the interlayer coupled optical response. From the distinct nano-FWM and -2PPL tip-sample distance dependent modification of interlayer and intralayer relaxation by tip-induced enhancement and quenching, we derive an interlayer energy transfer time of $\tau_{\mathrm{ET}} \sim (0.35^{+0.65}_{-0.15})$ ps consistent with recent reports. As a local probe technique, our approach highlights the ability to determine the intrinsic sample properties even in the presence of large sample heterogeneity, broadly applicable to a wide range of 2D heterostructures.

1 Introduction

Layer stacked two-dimensional (2D) van der Waals heterostructures exhibit novel magnetic [1], topological [2], superconducting [3], and other quantum phases that enable qualitatively new electronic, photonic, and optoelec-

This is the author manuscript accepted for publication and has undergone full peer review but has not been through the copyediting, typesetting, pagination and proofreading process, which may lead to differences between this version and the Version of Record. Please cite this article as doi: 10.1002/smll.202307345

tronic devices [4]. These functional properties emerge from a superposition of intrinsic intralayer interaction with extrinsic, orientation-dependent interlayer coupling [5, 6], giving rise to a Moiré-superlattice-controlled electronic band structure [7], distinct phonon dispersion [8], and enhanced electron-phonon coupling [9, 10]. Yet the mechanisms underlying interlayer coupling, including charge and energy transfer, are still poorly understood [11, 12, 13], particularly their sensitivity to spatial heterogeneities in the form of, e.g., defects, edges, grain boundaries, or strain.

In that regard, layered heterostructures of graphene with 2D transition metal dichalcogenides (TMDs) are of particular interest. Despite the absence of a Moiré band structure, the combination of the high electron mobility and long spin diffusion length of graphene with the direct and tunable bandgap of TMDs, and their strong spin-orbit coupling provides for a rich playground of properties [14, 15, 16] through current modulation [17], light-matter interaction [18, 19], photonic response [20, 21], spin-/valley-tronics [22, 23, 24, 25], neuromorphic memristors [26, 27], Rashba spin-orbit coupling [28, 29], and photoelectrochemical energy conversion and storage [30, 31]. In order to characterize the effect of interlayer coupling on these properties many studies have addressed the question of interlayer charge and energy transfer and their dynamics in these systems [32, 33, 12, 13]. Specifically, time- and angle-resolved photoemission spectroscopy (tr-ARPES) [34, 35, 36] and pump-probe time-resolved spectroscopy [37, 38, 39, 40, 41, 42, 43] have been used to measure the charge transfer dynamics. The timescales found range from 83 fs [37], 100's of fs [34, 35] to $\sim$1 ps [36, 38, 39] in WS_2/graphene, from sub-100 fs [40] to $\sim$0.5 ps [41], and varying with twist angle [42] in MoS_2/graphene, and 350 fs in WSe_2/graphene [43]. Similarly, theoretical studies [44] and time-resolved Raman and photoluminescence spectroscopy [45, 46] have addressed the energy transfer dynamics, finding timescales of few-ps in $MoSe_2$/graphene [44] and $\sim$4 ps in WS_2/graphene [45].

The range of timescales are in part attributed to variations in interlayer distance dependent on sample condition [12, 47, 32, 48, 49], and raises the question about the role of spatial heterogeneities. Already the distinction between interlayer charge and energy transfer in the competition with different intra- and interlayer radiative and non-radiative processes is difficult in general. Recent work extending ARPES to $\sim$500 nm spatial resolution highlights the sensitivity of exciton dynamics in TMDs with respect to a range of heterogeneities [50, 51].

Here, we perform spatio-spectral tip-enhanced nanoimaging of coherent four-wave mixing (FWM) and incoherent two-photon photoluminescence (2PPL) in WSe_2/graphene. We observe a high degree of spatial heterogeneity associated with folds, wrinkles, bubbles, and other defects, which we resolve with $\sim$50 nm spatial resolution. We isolate the homogeneous response in clean sampling regions and distinguish between charge versus energy transfer by inserting hexagonal boron nitride (h-BN) as an interlayer spacer selectively blocking the charge transfer channel. Based on the identification of energy transfer controlling the FWM response, we then take advantage of the tip-induced modification of the electron dynamics as a tool to separate competing relaxation pathways through their selective and tip-sample distance-dependent modification in z-scan nano-spectroscopy.

Combining this coupled rate equation model approach with multispectral FWM and 2PPL, we quantify the energy transfer time of $\tau_{\mathrm{ET}} \sim (0.35^{+0.65}_{-0.15})$ ps, consistent with an Auger-type process [52]. As a perspective, we discuss how the combination of tip-enhanced coherent FWM and incoherent 2PPL serve as a tool to investigate the nonlinear optical and electronic response, and their control through tip enhancement and material engineering on the nanoscale.

2 Experiment

Figure 1a-b show the experimental concept of adiabatic nanofocused FWM and 2PPL spectroscopy and imaging with few-femtosecond excitation provided by a Ti:sapphire oscillator with center wavelength at 800 nm as described previously [53, 54, 55, 56]. The excitation spectrum is cut with a longpass filter at 790 nm (see SI Figure S1). For the WSe_2 /graphene heterostructure, we transfer monolayer WSe_2 (top) onto 1-3 layer graphene (bottom). Since graphene is centrosymmetric, the angle between the WSe_2 and graphene will not significantly affect the charge and/or energy transfer dynamics [57]. An optical image of the sample is shown at the bottom of Figure 1a (for details see Experimental Section).

With the tip in shear-force feedback with the sample, Figure 1c shows the tip-scattered near-field emission spectra on the WSe_2 (top panel), graphene monolayer (middle panel), and the heterostructure (bottom panel) regions. For a more detailed signal analysis, we separate the overlapping 2PPL and FWM signals using double Voigt profiles (dashed lines). The incoherent 2PPL signal with peak at 750 nm is dominated by the direct band-gap transition A-exciton ($\sim$1.65 eV), scaling with the square of the pump power as expected [56]. It is accompanied by FWM which is also enhanced by resonant interaction with the A-exciton (see also SI Note 1) as recently demonstrated [56]. For discussion on the contribution of acoustic phonon resonances to our FWM signal, see SI Note 2. In contrast, the 2PPL signal is absent for graphene alone, as expected, and the signal consists purely of the FWM response [55]. For the heterostructure, both 2PPL and FWM are present, yet with a reduced 2PPL intensity due to quenching by graphene [48, 45, 12, 58, 59, 46, 60].

Figure 1d illustrates the different pathways for 2PPL and FWM generation from WSe_2 and graphene. The signal from the heterostructure is controlled by both the monolayer responses and the interlayer coupling with possible charge transfer (CT) and energy transfer (ET). ET in 2D heterostructures is commonly described as Förster-type energy transfer, which is a long-range interaction through dipole-dipole coupling, which can occur even between two layers separated by > 10 nm [49]. We provide additional details on other possible ET mechanisms in the Discussion section. As illustrated in Figure 1b (bottom panel) CT and ET would each manifest differently in the FWM response, and would each be affected differently by insertion of a thin hBN sheet. Relative to isolated WSe_2 on SiO_2 on the left or isolated graphene on SiO_2 on the right, the plus, minus, and circle symbols in Figure 1b represent the enhanced, quenched, and unaffected (respectively) FWM signal from various combinations of WSe_2 , graphene, and hBN. For example, hBN/graphene regions exhibit high FWM signals (rep-

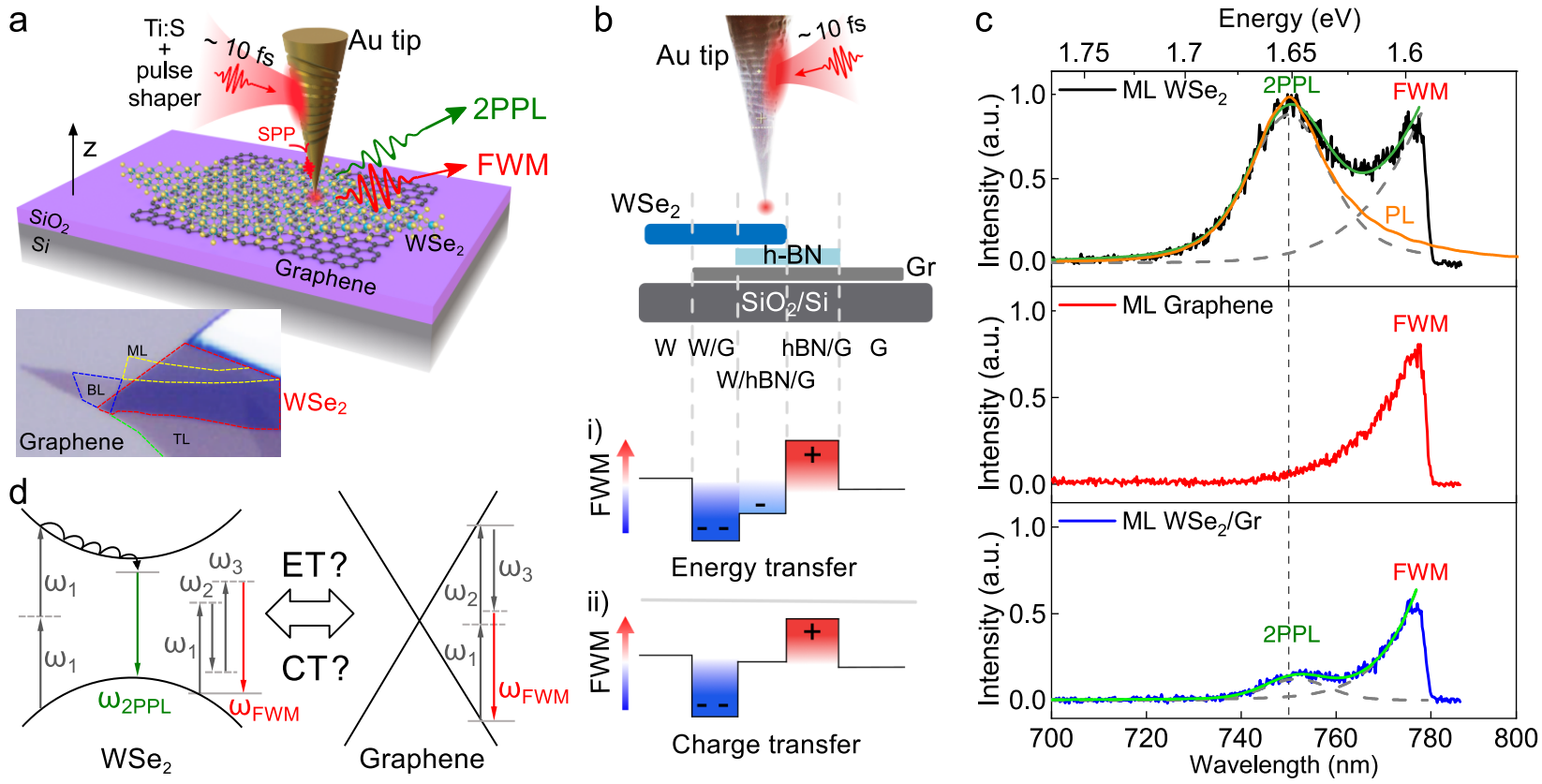

Fig. 1: Nanofocusing-excited spectroscopy of WSe_2 /graphene heterostructure. (a) Schematic of grating-coupling and femtosecond adiabatic nanofocusing with pulse shaping for nanolocalized excitation on WSe_2 /graphene heterostructure with sub-nanometer tip-sample distance control. (b) Excitation on WSe_2 /hBN/graphene heterostructure with predicted FWM intensities of different heterostructure regions when compared to WSe_2 alone in i) the energy transfer (ET) dominated regime, and ii) in the charge transfer (CT) dominated regime. Positive and negative signs indicate expected FWM enhancement and quenching, respectively. (c) Tip-enhanced 2PPL and FWM (black) from monolayer (ML) WSe_2 , FWM (red) from monolayer graphene, 2PPL and FWM (blue) from monolayer WSe_2 /monolayer graphene heterostructure, along with corresponding fits. (d) Pathways of 2PPL and FWM emissions from WSe_2 , and FWM emission pathway from graphene.

resented with a plus sign in Figure 1b due to the highly ordered hBN leading to increased coherence times. In WSe_2 /graphene regions, either CT or ET effects quench the FWM signal. If CT dominates the interlayer interactions we would expect the presence of an (> 3 nm) hBN spacer to suppress this quenching effect. Conversely, if ET dominates then its long-range coupling of up to tens of nm would be less sensitive to the hBN spacer layer and the graphene FWM would still be quenched by WSe_2 regardless of the hBN.

3 Results

3.1 FWM and 2PPL nanoimaging of WSe_2 /graphene heterostructure

We perform systematic FWM and 2PPL nano-imaging of the WSe_2 /graphene heterostructure to analyze the signal dependence on structural heterogeneities, to locate clean homogeneous sample regions, and thus determine the intrinsic sample response in local probe spectroscopy on these selected regions. **Figure 2** show near-field images of nano-FWM (a) and nano-2PPL (b) for the WSe_2 on mono- and multi-layer graphene heterostructure for the

region highlighted in the AFM topography image (c). The near-field images reveal a high degree of heterogeneity with ~50 nm spatial resolution (see SI Figure S2), in contrast to conventional far-field micro-FWM and micro-2PPL imaging which exhibits only a small degree of spatial variation (see SI Figure S3).

Overall, the FWM signal increases with increasing graphene layer thickness from mono- (1G), to bi- (2G), and tri-layer (3G) as expected [55]. Heterogeneities in the form of bubbles generally decrease the FWM signal [61]. For the WSe_2 /graphene heterostructures W/1G and W/2G, the FWM signal intensities are below those of 1G and 2G, respectively, while the W/3G signal is comparable to 3G. These trends are summarized in Figure 2d which is obtained from spatial averaging across the respective regions. A higher degree of heterogeneity is observed for W/nG compared to nG which we attribute to the additional sensitivity with respect to interlayer spacing. In contrast, the 2PPL signal is significantly quenched in W/1G compared to monolayer WSe_2 , with little additional signal change for W/2G and W/3G.

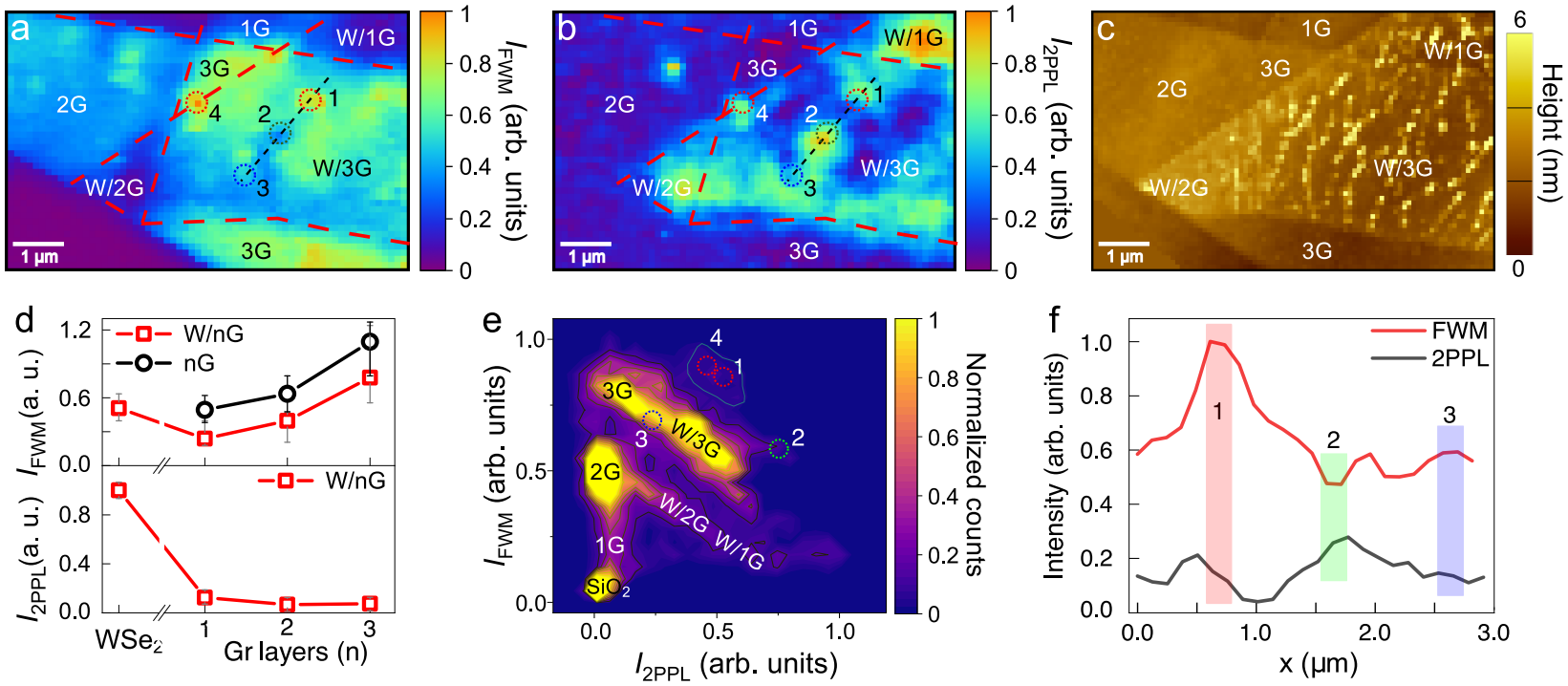

Fig. 2: Nano-images highlighting the influence of heterogeneities on WSe_2 /nGr. Nano-FWM (a) and nano-2PPL (b) imaging, and AFM topography (c). (d) Layer dependence of nano-FWM and nano-2PPL intensities extracted from (a-b). (e) Corresponding FWM-2PPL correlation plot, with sample segments and individual heterogeneities labeled. (f) Comparison of FWM and 2PPL intensities at spots 1-3.

Significantly, we observe that the heterostructure areas which exhibit a higher FWM signal (W/1G, W/2G and W/3G) have a weaker 2PPL signal. This general anti-correlation is seen in Figure 2e as the diagonals in the FWM versus 2PPL plane, with the respective sample segments labeled correspondingly. The behavior of four selected sample locations 1-4 is highlighted in Figure 2a, b, and e, with uncorrelated (1), anti-correlated behavior (2,3), and correlated (4) relationships. Figure 2f shows corresponding FWM line profiles along the dashed lines indicated in Figure 2a-b through the defects 1, 2, and 3.

We consider five possible types of topological heterogeneities, including folds, wrinkles, and bubbles, and

their expected impact on the FWM and interlayer dynamics (see SI Figure S4 for details). The observation of a smaller spatial variation in FWM compared to the heterogeneity observed in AFM topography within the spatial resolution of $\sim$50 nm suggests that the majority of structural features observed in AFM are not folds or wrinkles, but bubbles or contaminations.

3.2 WSe_2 and graphene with h-BN spacer

In order to investigate the effect of layer coupling for the purpose of identifying the coupling mechanism, we then study a new sample with hBN as a spacer layer between monolayer WSe_2 (top) and graphene (bottom) and image segments of 1G, 2G, W/hBN, W/1G, W/2G, hBN/1G, hBN/2G, W/hBN/1G, and W/hBN/2G as shown in **Figure 3** with nano-FWM (b and c) of two areas indicated by white dashed rectangles in the AFM topography (d) (for corresponding far-field FWM and 2PPL images see SI Figure S5).

To visualize the FWM intensity change with number of graphene layers, and with/without hBN, we summarize the main trends for homogeneous sample areas in Figure 3e. As expected, we observe a stronger FWM response for hBN/graphene areas (hBN/1G, hBN/2G) compared to graphene on SiO_2 alone (1G, 2G). This is due to hBN reducing the amount of defects on the graphene surface thus efficiently reducing heterogeneity-introduced dephasing (Coulomb scattering) [62], as well as neutralizing the graphene doping level [46], which together lead to a higher $\chi^{(3)}$ response [63]. Further, from the relative increase in FWM intensity with increasing graphene layer number under otherwise identical conditions for both isolated graphene as well as WSe_2 /graphene, we infer that the overall FWM signal is dominated by contributions from graphene over WSe_2 .

Significantly, the ratio $\frac{I_{\mathrm{FWM}}(1\mathrm{G})}{I_{\mathrm{FWM}}(\mathrm{W}/1\mathrm{G})}$ is larger with the hBN spacer layer than without it (Figure 3e). This results from the combined effect of the hBN increasing the FWM signal as described above and the graphene interaction with WSe_2 decreasing the FWM signal regardless of the hBN spacer. The ratio $\frac{I_{\mathrm{FWM}}(2\mathrm{G})}{I_{\mathrm{FWM}}(\mathrm{W}/2\mathrm{G})}$, however, is smaller with the hBN spacer layer than without it, showing that hBN can efficiently decrease the WSe_2 quenching of the graphene FWM. This decrease of FWM is observed in all W/hBN/nG regions, with the effect still discernible at $\sim$3.3 nm hBN thickness (corresponding to 8 layers). This implies that the FWM quenching in W/nG is *not* due to *charge transfer*, which would be blocked by a hBN spacer thicker than 1 nm [12, 33]. We thus attribute the quenching of the graphene FWM by WSe_2 to long-range *energy transfer*. Similar quenching behaviors can be found from far-field FWM, 2PPL, and PL images (see SI Figure S5), which also suggest a long-range energy transfer between WSe_2 and graphene. Of particular note, the FWM intensities of W/1G and W/hBN/1G are similar, suggesting that energy transfer dominates in both scenarios at a similar rate.

In terms of the heterogeneities in FWM, we observe both correlated and uncorrelated behavior with topography (Figure 3f). We observe enhanced FWM emissions from what seems to be wrinkles (profile 1-2), a bubble (profile 3) and a fold (profile 4). However, not all topographic features are associated with enhanced FWM emission which shows that the FWM is not uniformly and predictably affected by strain.

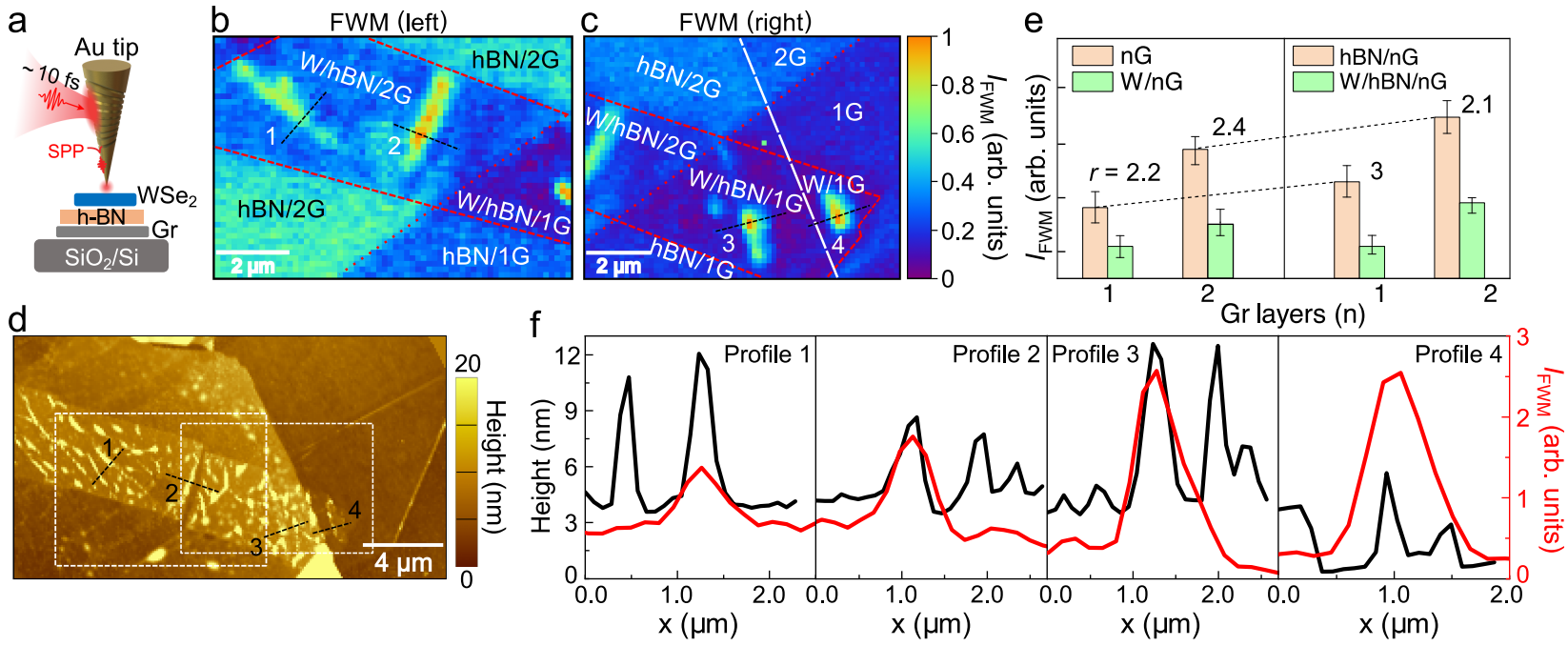

Fig. 3: Nanoimaging with hBN (∼3.3 nm) between WSe_2 and graphene. (a) Nanofocusing on WSe_2 /hBN/graphene. (b-c) FWM nano-imaging of two overlapping regions, the dashed lines indicate the physical boundaries of different areas, which are labeled. (d) Corresponding AFM topography image with white dashed rectangles indicating the two nano-imaging scan areas in (b-c). (e) Layer dependence of FWM intensity extracted from (b-c). The r is defined by the ratio of FWM intensity of nG to W/nG and hBN/nG to W/hBN/nG. (f) Line profiles extracted from (b-d) showing FWM intensities together with the corresponding topography variations exemplifying the response of correlated and uncorrelated FWM intensity with wrinkles, folds, and bubbles.

3.3 PL quenching mechanisms

In TMD/graphene heterostructures both charge- and energy-transfer processes have been previously proposed to explain PL quenching of the TMD emission [46, 39, 38]. While PL quenching is typically seen as an indicator of interlayer charge transfer, energy transfer also significantly influences the quenching process, even over a large range, via strong dipole-dipole interactions [64]. For example, non-radiative exciton energy transfer from WS_2 to graphene has been shown to dominate in the pronounced PL quenching and reduction of exciton lifetimes [59]. In a separate WS_2 /graphene study, the quenching of both the PL and 2D Raman mode of WS_2 was observed using time-resolved Raman experiments. The increase in the numerically simulated electron temperature was attributed to energy transfer from WS_2 to graphene, with near-unity efficiency [45]. Indeed, a study of $MoSe_2$ /graphene suggests that a net charge transfer has no effect on the nearly complete graphene-induced PL quenching, which instead is dominated by energy transfer (either by electron exchange or dipole-dipole interaction) [32]. Recent optical spectroscopy and electrical measurements in $MoSe_2$ /graphene heterostructures have demonstrated significant PL quenching, which is weakened by an h-BN interlayer and well described by an energy transfer model [58].

One previous study observed charge transfer through a hBN layer in the quenching and blueshift of the A_{1g} Raman mode in a WS_2 /hBN/graphene heterostructure [65], however, the observed charge- and Dexter-transfer effects were mediated through defects in the hBN spacer layer. Because we observe uniform FWM enhancement

in hBN/graphene regions, the hBN in our sample evidently has few defects and does not support such defect-assisted charge transfer processes. Therefore, this defect-mediated charge transfer description does not apply to our WSe_2 /hBN/graphene heterostructure.

Our work therefore confirms previous findings that energy transfer is the dominant interlayer interaction that leads to the efficient PL quenching of TMDs on graphene, assigned to picosecond energy transfer mediated by longer-range dipole-dipole (Förster-type) interactions [60, 66].

3.4 FWM and 2PPL z-scan nanospectroscopy

Following the verification that the quenching of the FWM signal is dominated by energy transfer, we proceed to determine its rate. For this purpose, we first prepare a similar sample containing larger regions of smooth topography and less structural heterogeneities. **Figure 4**a shows AFM topography with nano FWM raster sampling (as a compromise between spatial resolution, sample drift, and tip degradation) to identify areas with both homogeneous topography and FWM response. To then determine the associated intrinsic energy transfer time in these areas, we perform z-scan spectroscopy measuring the tip-sample distance-dependent response of 2PPL (b) and FWM (c) with examples shown for the sample area indicated by the red square in Figure 4a. As a reference, we performed the same measurement on bare homogeneous monolayer WSe_2 , as shown in Figure 4d-e.

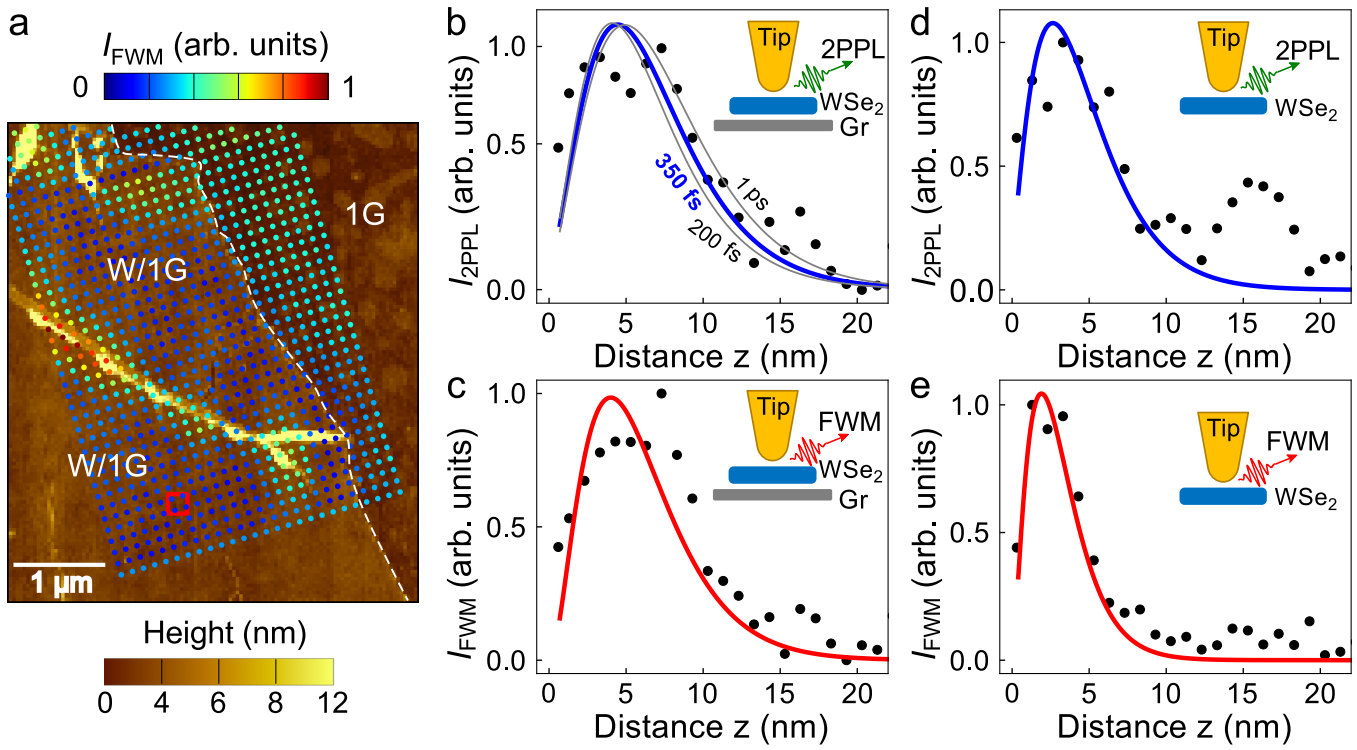

Fig. 4: 2PPL and FWM z-scan nano-spectroscopy. (a) AFM topography of W/1G and 1G sample, with nano-FWM raster sampling to identify regions with homogeneous FWM response. (b-c) z-scan spectroscopy of nano-2PPL (b) and nano-FWM (c) of W/1G (red square in a). Numerical fit based on a coupled rate equation model with best fit to an energy transfer times scale of $\tau_{ET} \sim (0.35^{+0.65}_{-0.15})$ ps. (d-e) Corresponding reference measurement on homogeneous WSe_2 monolayer.

The evolution of the 2PPL and FWM signal with tip-sample distance is determined by a competition between

the tip-enhanced excitation and the combination of radiative and non-radiative relaxation. For $z > 5$ nm, 2PPL and FWM increase with decreasing distance due to the tip-sample coupled local field enhancement [67]. However, for distances $z < 5$ nm the onset of dipole-dipole coupling between tip and sample gives rise to increased nonradiative relaxation that begins to outcompete the radiative decay. Here, 2PPL and FWM polarization transfer into the metallic tip is followed by quenching due to ultrafast ohmic Drude damping [68].

3.5 Model of 2PPL and FWM distance curves

Modeling the 2PPL and FWM distance curves, based on existing knowledge of radiative lifetimes we can estimate the interlayer energy transfer time in the WSe_2 /graphene heterostructure [69]. We use a coupled rate equation model to describe the competing decay pathways of both the exciton population and coherent electron polarization. The 2PPL intensity is proportional to the exciton population in the WSe_2 monolayer N_{W}, and evolves as

$$\frac{\mathrm{d}N_W}{\mathrm{d}t} = F_{\mathrm{W}} - (\Gamma_{\mathrm{W}}^{\mathrm{rad}} + \Gamma_{\mathrm{W}}^{\mathrm{nrad}} + \Gamma_{\mathrm{ET}}^{\mathrm{nrad}})N_{\mathrm{W}} \tag{1}$$

with F_{W} the exciton excitation rate, $\Gamma_{\mathrm{W}}^{\mathrm{rad}}$ and $\Gamma_{\mathrm{W}}^{\mathrm{nrad}}$ the radiative and non-radiative decay rates, respectively, and $\Gamma_{\mathrm{ET}}^{\mathrm{nrad}}$ the non-radiative energy transfer rate into the graphene layer (see model in **Figure 5**a).

Because excitation occurs directly through the nanofocused laser field at the tip apex, the excitation rate will rise exponentially on a characteristic field localization length scale D [70]. Therefore, the 2PPL excitation rate, with a power dependence of 2, will scale as $F_{\mathrm{W}} \propto e^{-2z/D}$. The radiative decay rate $\Gamma_{\mathrm{W}}^{\mathrm{rad}}$ of excitons in WSe_2 is fixed to $1/\Gamma_{\mathrm{W}}^{\mathrm{rad}} = 0.7$ ns based on previously measured values [69, 71, 72, 73] and as expected for radiative dipole emission in the near-IR spectral range. Meanwhile, the nonradiative decay rate $\Gamma_{\mathrm{W}}^{\mathrm{nrad}}$ is the sum of an intrinsic decay rate $\Gamma_{\mathrm{W}}^{\mathrm{nrad,0}}$ and an additional distance-dependent term arising from dipole-dipole coupling to the tip, $\Gamma_{\mathrm{W}}^{\mathrm{nrad,tip}} \propto (R/(z+\delta z))^l$, scaling with tip radius R, minimal tip-exciton separation δz, and following a power law with $l \sim 2$. We assume $1/\Gamma_{\mathrm{W}}^{\mathrm{nrad,0}}$ = 2.6 ps based on previous measurements [69], and consistent with the generally low quantum yield ($\sim$0.1%) for samples prepared under similar conditions [73, 74, 75].

Similarly, the FWM intensity I_{FWM} will depend on the coherent electron polarization and thus will be determined by the ratio of the excitation and relaxation rate:

$$I_{\mathrm{FWM}} = F_{\mathrm{FWM}}/(R/z)^l \tag{2}$$

with F_{FWM} the excitation rate of electronic coherence, and $(R/z)^l$ the tip-induced decoherence following the same $l \sim 2$ power law as the 2PPL case. The excitation rate will again decay exponentially with distance from the tip, but as $F_{\mathrm{FWM}} \propto e^{-3z/D}$ due to FWM being a third order process.

We then apply this model to fit the approach curves in Figure 4b-e, with analytical solutions to Equations 1-2 for the 2PPL and FWM intensities, and globally minimize the residuals of all cases (for details see SI Note3).

We find the best fit using $\Gamma_{\mathrm{ET}}^{\mathrm{nrad}}$=1/350 fs^{-1} with estimated asymmetric statistical uncertainty corresponding to $\tau_{\mathrm{ET}} \sim(0.35^{+0.65}_{-0.15})$ ps. For additional details on the fitting procedure and analysis see SI Note 3 and Discussion Section.

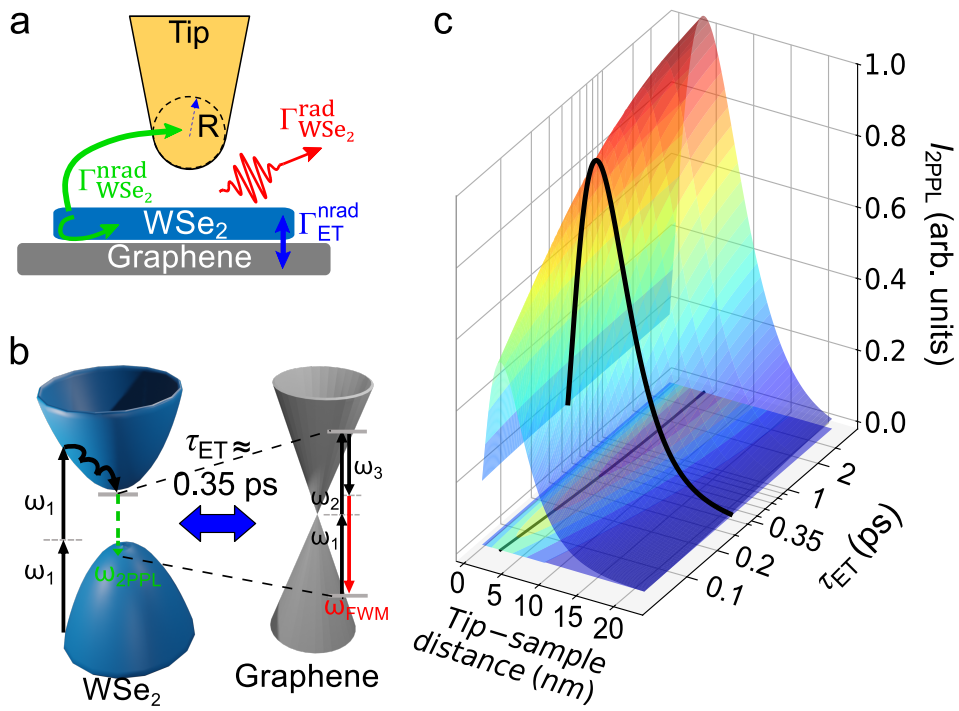

Fig. 5: Model parameters controlling tip-sample and interlayer coupling. (a) Non-radiative and radiative decay channels. (b) Optical excitation, relaxation, and energy transfer pathways. (c) Simulation of 2PPL emission intensity for τ_{ET} ranging from 50 fs to 3.5 ps with best fit for 350 fs (black).

4 Discussion

We discuss the energy transfer mechanisms.

The existing body of literature describing energy transfer timescales is inconclusive. Measured timescales vary widely and are ascribed to multiple different mechanisms. We compare our estimated energy transfer time of ∼0.35 ps with results from similar heterostructures with different energy transfer mechanisms, including Förster- and Dexter-type energy transfer. Förster-type energy transfer occurs when an electron-hole pair, or exciton, within one of the layers recombines non-radiatively, transferring the energy into the other layer through dipole-dipole coupling where it then leads to a secondary excitation [76, 77]. In contrast, Dexter-type energy transfer involves correlated interlayer transfer of both electrons and holes, yet without a net charge transfer [78, 77]. At short distances both Dexter- and Förster-type energy transfer can occur, making them difficult to distinguish.

For example, in a recent study of a MoS_2 /graphene heterostructure, electrical measurements and Raman/PL analyses found that energy transfer dominates over charge transfer [46], but the different mechanisms of Dexter or Förster type energy transfer could not be distinguished. Similarly, a study of a WS_2 /graphene heterostructure measured a 4 ps energy transfer time by photo-exciting the WSe_2 and WSe_2 /graphene separately, agreeing with predictions for the Förster and Dexter energy transfer timescales [45]. Meanwhile, a systematic comparison of

interlayer electron/hole transfer and energy transfer mechanisms in $MoSe_2$ /graphene heterostructures suggested that interlayer interactions are dominated by energy transfer either in the form of electron/hole exchange (Dexter) or dipole-dipole interaction (Förster) [32]. From this range of studies investigating 2D heterostructures we can conclude that energy transfer is a significant interaction mechanism between TMDs and graphene and occurs on few ps timescales.

It is worth mentioning that theory predicts that Förster-type energy transfer between graphene and TMDs occurs on 5 ps timescales due to the energy-momentum conservation between participating quasiparticles [44]. The associated dephasing rate was shown to decrease with increasing interlayer spacing due to a broadening effect during the exciton transfer energy to graphene, leading to a decrease in FWM intensity. This prediction is consistent with our FWM quenching observed in WSe_2 /graphene. Förster dipole-dipole interactions can thus explain the long-range coupling we observed in the WSe_2 /hBN/graphene regions. However, this observed long range interaction is not consistent with Dexter-type transfer which requires small interlayer spacing to facilitate exciton tunneling.

Other mechanisms besides Dexter- and Förster-type energy transfer are also possible. For example, in a metal/CdO semiconductor structure, the photo-excited hot electrons in the metal couple excess energy into the CdO electron subsystem due to the strong overlap of the electronic wavefunctions between the two materials through ballistic thermal injection with a $\sim$3 ps timescale [79].

More recently, energy-transfer timescales as fast as $\sim$70 fs were observed experimentally [52]. To explain this unusually fast dynamics, a fast Auger-type mechanism was theoretically proposed as a form of dipole (WSe_2)-monopole (graphene) interaction, and suggested to dominate over conventional Förster- and Dexter-type interactions. This dipole-monopole coupled Auger transfer was predicted to occur on 270 fs timescales which could be consistent with our $\sim$0.35 ps rate, suggesting indeed that such a process contributes to the interlayer energy transfer dynamics. From our observed timescale and long-range interactions, we therefore conclude that energy transfer dominates over charge transfer in WSe_2 /graphene heterostructures. However, due to the uncertainty in our estimated energy transfer timescale and the range of values in the literature, further work would be needed to truly conclude whether the energy transfer arises from Förster transfer, Auger transfer, or a combination of both.

5 Summary and Perspective

In summary, we performed FWM and 2PPL micro- and nano-imaging based on few-fs adiabatic nanofocusing to investigate the nonlinear optical response of WSe_2 /graphene heterostructures. We observe tip-induced enhancement and quenching of FWM and 2PPL, along with an anticorrelation between the two nonlinear signals and nanoscale heterogeneity on the length scale of $\sim$50 nm. To determine the nature of the interlayer coupling between graphene and monolayer WSe_2 , we insert hBN spacer layers and thus attribute the observed long-range interaction to a Förster-type and/or Auger-type energy transfer. From z-scan spectroscopy of nano-FWM and

-2PPL in selected homogenous sample regions, we derived an energy transfer time between WSe_2 and graphene of $\tau_{\mathrm{ET}} \sim (0.35^{+0.65}_{-0.15})$ ps.

This work highlights the risk of spatially averaging over the wide range of possible structural heterogeneities in conventional spectroscopy of devices prepared by simple exfoliation under ambient conditions. Yet we demonstrate that, even for spatially heterogeneous systems, nanoscale mapping and local probe spectroscopy can nevertheless resolve the intrinsic material response in selected sub-regions. This is particularly relevant for understanding the underlying interplay between intra- and inter-layer excitation and relaxation processes, as well as the intrinsic coherence and population dynamics in topological, spin, magnetic, superconducting, and other emergent 2D quantum materials that arise from twist angle dependent homo- or hetero-multilayers which are particularly sensitive with respect to structural heterogeneities. In that regard, tip-enhanced spectroscopy and imaging can contribute with controllable modification of these pathways using z-scan spectroscopy [80], nano-cavity Purcell enhancement [81], or multi-modal coherent and incoherent nonlinear spectroscopy [61], while simultaneously identifying and avoiding the extrinsic effects of material defects and heterogeneities.

6 Methods

Samples:

The graphene was mechanically exfoliated from Kish graphite crystals (Graphene Supermarket, Ronkonkoma, NY, USA) onto a Si substrate with a 90 nm layer of SiO_2 . WSe_2 was exfoliated from bulk WSe_2 crystals (2Dsemiconductors, Scottsdale, AZ, USA) and stacked onto the graphene using a polycarbonate-based dry-transfer technique [82].

Experimental setup:

Nano-focusing gold tips were electrochemically etched, then engraved with the plasmonic grating coupler using focused ion beam (FIB) milling [83]. The tips were mounted on a shear-force tuning-fork-based atomic force microscope (AFM) with feedback controlled by a three axis piezo stage (Physik Instrumente, P-517) and an AFM controller (RHK Technology, R9plus) [84]. The grating coupled broad-band femtosecond pulses from a Ti:sapphire oscillator (nominal pulse duration $\sim$10 fs) spatially compress during propagation as a result of the divergence of the effective index of refraction of the plasmon wave with decreasing cone radius [85]. The dispersion during propagation is compensated by a home-built pulse shaper, based on a dual-mask spatial light modulator (CRi SLM640) in the Fourier plane of a $4f$ system, using multiphoton intrapulse interference phase scans (MIIPS) with second-harmonic generation (SHG) from the tip apex serving as feedback [85].

The experimental setup employed to measure the emission signal from the tip apex included a spatial filter

to cut off the fundamental signal, and a spectrometer equipped with a thermoelectrically cooled CCD detector (ProEM+:1600 eXcelon3, Princeton Instruments) with a focal length of 500 mm (SpectraPro 500i, Princeton Instruments) to detect the nonlinear signals.

Supporting Information

Supporting Information is available from the Wiley Online Library or from the author.

Acknowledgements

W.L., B.G.W., and M.B.R. acknowledge funding from the US Department of Energy, Office of Basic Sciences, Division of Material Sciences and Engineering, under award no. DESC0008807. A.B. acknowledges funding from the Air Force Office for Scientific Research Grant No. FA9550-21-1-0272 and National Science Foundation Award No. 1936276. W.L. and T.J. acknowledge support from the National Natural Science Foundation of China (62175188, 62005198) and the Science and Technology Commission of Shanghai Municipality (23ZR1465800, 23190712300). W.L. and X.C. acknowledge support from the National Natural Science Foundation of China (61925504, 62020106009, 6201101335) and the Special Development Funds for Major Projects of Shanghai Zhangjiang National Independent Innovation Demonstration Zone (ZJ2021-ZD-008). W.L. acknowledges a fellowship from the International Postdoctoral Exchange Fellowship Program of the Chinese Ministry of Human Resources and Social Security (MoHRSS) (20190052 to W. L.). The authors acknowledge the assistance of Yibo Yang (Department of Computer Science, University of Colorado Boulder) on computational data analysis. We thank Shuo Dong, Malte Selig, Andreas Knorr, Ralph Ernstorfer, Ermin Malic and Marcel Reutzel for helpful discussions.

Author contributions

W.L., T.J., and M.B.R. conceived and designed the experiments. R. S. fabricated the samples. W.L. conducted the measurements with support from B.G.W. and guidance from T.J. and M.B.R.. A.B. provided the theoretical model. W.L., B.G.W., A.B., and M.B.R. discussed and wrote the manuscript with the help of all authors. All the authors read and provided comments on the manuscript.

Conflict of Interest

The authors declare no conflict of interest.

References

[1] D. Zhong, K. L. Seyler, X. Linpeng, N. P. Wilson, T. Taniguchi, K. Watanabe, M. A. McGuire, K.-M. C. Fu, D. Xiao, W. Yao, X. Xu, *Nat. Nanotechnol.* **2020**, *15* 187.

[2] J. Wu, F. Liu, M. Sasase, K. Ienaga, Y. Obata, R. Yukawa, K. Horiba, H. Kumigashira, S. Okuma, T. Inoshita, H. Hosono, *Sci. Adv.* **2019**, *5* eaax9989.

[3] Y. Cao, V. Fatemi, S. Fang, K. Watanabe, T. Taniguchi, E. Kaxiras, P. Jarillo-Herrero, *Nature* **2018**, *556* 43.

[4] K. S. Novoselov, A. Mishchenko, A. Carvalho, A. H. Castro Neto, *Science* **2016**, *353* aac9439.

[5] A. Ciarrocchi, F. Tagarelli, A. Avsar, A. Kis, *Nat. Rev. Mater.* **2022**, *7* 449.

[6] D. Huang, J. Choi, C.-K. Shih, X. Li, *Nat. Nanotechnol.* **2022**, *17* 227.

[7] G. Chen, L. Jiang, S. Wu, B. Lyu, H. Li, B. L. Chittari, K. Watanabe, T. Taniguchi, Z. Shi, J. Jung, Y. Zhang, F. Wang, *Nat. Phys.* **2019**, *15* 237.

[8] J. Quan, L. Linhart, M.-L. Lin, D. Lee, J. Zhu, C.-Y. Wang, W.-T. Hsu, J. Choi, J. Embley, C. Young, T. Taniguchi, K. Watanabe, C.-K. Shih, K. Lai, A. H. MacDonald, P.-H. Tan, F. Libisch, X. Li, *Nat. Mater.* **2021**, *20* 1100.

[9] Y. W. Choi, H. J. Choi, *Phys. Rev. Lett.* **2021**, *127* 167001.

[10] C. Jin, J. Kim, J. Suh, Z. Shi, B. Chen, X. Fan, M. Kam, K. Watanabe, T. Taniguchi, S. Tongay, A. Zettl, J. Wu, F. Wang, *Nat. Phys.* **2017**, *13* 127.

[11] C. Jin, E. Y. Ma, O. Karni, E. C. Regan, F. Wang, T. F. Heinz, *Nat. Nanotechnol.* **2018**, *13* 994.

[12] C. Bradac, Z.-Q. Xu, I. Aharonovich, *Nano Lett.* **2021**, *21* 1193.

[13] Z. Hu, X. Liu, P. L. Hernández-Martínez, S. Zhang, P. Gu, W. Du, W. Xu, H. V. Demir, H. Liu, Q. Xiong, *InfoMat* **2022**, *4* e12290.

[14] S. J. White, T. Yang, N. Dontschuk, C. Li, Z.-Q. Xu, M. Kianinia, A. Stacey, M. Toth, I. Aharonovich, *Light Sci. Appl.* **2022**, *11* 186.

[15] K. Kim, S. Larentis, B. Fallahazad, K. Lee, J. Xue, D. C. Dillen, C. M. Corbet, E. Tutuc, *ACS Nano* **2015**, *9* 4527.

[16] M. Yankowitz, S. Larentis, K. Kim, J. Xue, D. McKenzie, S. Huang, M. Paggen, M. N. Ali, R. J. Cava, E. Tutuc, B. J. LeRoy, *Nano Lett.* **2015**, *15* 1925.

[17] T. Georgiou, R. Jalil, B. D. Belle, L. Britnell, R. V. Gorbachev, S. V. Morozov, Y.-J. Kim, A. Gholinia, S. J. Haigh, O. Makarovsky, L. Eaves, L. A. Ponomarenko, A. K. Geim, K. S. Novoselov, A. Mishchenko, *Nat. Nanotechnol.* **2013**, *8* 100.

[18] L. Britnell, R. M. Ribeiro, A. Eckmann, R. Jalil, B. D. Belle, A. Mishchenko, Y.-J. Kim, R. V. Gorbachev, T. Georgiou, S. V. Morozov, A. N. Grigorenko, A. K. Geim, C. Casiraghi, A. H. Castro Neto, K. S. Novoselov, *Science* **2013**, *340* 1311.

[19] Y. Jiang, S. Chen, W. Zheng, B. Zheng, A. Pan, *Light Sci. Appl.* **2021**, *10* 72.

[20] M. Massicotte, P. Schmidt, F. Vialla, K. G. Schädler, A. Reserbat-Plantey, K. Watanabe, T. Taniguchi, K.-J. Tielrooij, F. H. Koppens, *Nat. Nanotechnol.* **2016**, *11* 42.

[21] F. Wang, T. Zhang, R. Xie, Z. Wang, W. Hu, *Nat. Commun.* **2023**, *14* 2224.

[22] B. Yang, M.-F. Tu, J. Kim, Y. Wu, H. Wang, J. Alicea, R. Wu, M. Bockrath, J. Shi, *2D Mater.* **2016**, *3* 031012.

[23] T. S. Ghiasi, J. Ingla-Aynés, A. A. Kaverzin, B. J. Van Wees, *Nano Lett.* **2017**, *17* 7528.

[24] C. Safeer, J. Ingla-Aynés, F. Herling, J. H. Garcia, M. Vila, N. Ontoso, M. R. Calvo, S. Roche, L. E. Hueso, F. Casanova, *Nano Lett.* **2019**, *19* 1074.

[25] J. F. Sierra, J. Fabian, R. K. Kawakami, S. Roche, S. O. Valenzuela, *Nat. Nanotechnol.* **2021**, *16* 856.

[26] T. Li, J. Miao, X. Fu, B. Song, B. Cai, X. Ge, X. Zhou, P. Zhou, X. Wang, D. Jariwala, W. Hu, *Nat. Nanotechnol.* **2023**, *18* 1303.

[27] X. Fu, T. Li, B. Cai, J. Miao, G. N. Panin, X. Ma, J. Wang, X. Jiang, Q. Li, Y. Dong, C. Hao, J. Sun, H. Xu, Q. Zhao, M. Xia, B. Song, F. Chen, X. Chen, W. Lu, W. Hu, *Light Sci. Appl.* **2023**, *12* 39.

[28] B. Yang, M. Lohmann, D. Barroso, I. Liao, Z. Lin, Y. Liu, L. Bartels, K. Watanabe, T. Taniguchi, J. Shi, *Phys. Rev. B* **2017**, *96* 041409.

[29] T. Wakamura, F. Reale, P. Palczynski, M. Zhao, A. Johnson, S. Guéron, C. Mattevi, A. Ouerghi, H. Bouchiat, *Phys. Rev. B* **2019**, *99* 245402.

[30] H. Wang, H. Feng, J. Li, *Small* **2014**, *10* 2165.

[31] C. Li, Q. Cao, F. Wang, Y. Xiao, Y. Li, J.-J. Delaunay, H. Zhu, *Chem. Soc. Rev.* **2018**, *47* 4981.

[32] G. Froehlicher, E. Lorchat, S. Berciaud, *Phys. Rev. X.* **2018**, *8* 011007.

[33] Z.-Q. Xu, N. Mendelson, J. A. Scott, C. Li, I. H. Abidi, H. Liu, Z. Luo, I. Aharonovich, M. Toth, *2D Mater.* **2020**, *7* 031001.

[34] R. Krause, M. Chávez-Cervantes, S. Aeschlimann, S. Forti, F. Fabbri, A. Rossi, C. Coletti, C. Cacho, Y. Zhang, P. E. Majchrzak, R. T. Chapman, E. Springate, I. Gierz, *Front. Phys.* **2021**, *9* 668149.

[35] R. Krause, S. Aeschlimann, M. Chávez-Cervantes, R. Perea-Causin, S. Brem, E. Malic, S. Forti, F. Fabbri, C. Coletti, I. Gierz, *Phys. Rev. Lett.* **2021**, *127* 276401.

[36] S. Aeschlimann, A. Rossi, M. Chávez-Cervantes, R. Krause, B. Arnoldi, B. Stadtmüller, M. Aeschlimann, S. Forti, F. Fabbri, C. Coletti, I. Gierz, *Sci. Adv.* **2020**, *6* eaay0761.

[37] Z. Song, H. Zhu, W. Shi, D. Sun, S. Ruan, *Optik* **2018**, *174* 62.

[38] J. He, N. Kumar, M. Z. Bellus, H.-Y. Chiu, D. He, Y. Wang, H. Zhao, *Nat. Commun.* **2014**, *5* 5622.

[39] L. Yuan, T.-F. Chung, A. Kuc, Y. Wan, Y. Xu, Y. P. Chen, T. Heine, L. Huang, *Sci. Adv.* **2018**, *4* e1700324.

[40] Z. Xu, Z. Liu, D. Zhang, Z. Zhong, T. B. Norris, *Appl. Phys. Lett.* **2021**, *119* 093102.

[41] Y. Zou, Q.-S. Ma, Z. Zhang, R. Pu, W. Zhang, P. Suo, K. Sun, J. Chen, D. Li, H. Ma, X. Lin, Y. Leng, W. Liu, J. Du, G. Ma, *J. Phys. Chem. Lett.* **2022**, *13* 5123.

[42] D. Luo, J. Tang, X. Shen, F. Ji, J. Yang, S. Weathersby, M. E. Kozina, Z. Chen, J. Xiao, Y. Ye, T. Cao, G. Zhang, X. Wang, A. M. Lindenberg, *Nano Lett.* **2021**, *21* 8051.

[43] L. Zhang, Z. Chen, R. Zhang, Y. Tan, T. Wu, M. Shalaby, R. Xie, J. Xu, *ACS Appl. Mater. Interfaces* **2019**, *11* 47501.

[44] M. Selig, E. Malic, K. J. Ahn, N. Koch, A. Knorr, *Phys. Rev. B* **2019**, *99* 035420.

[45] C. Ferrante, G. Di Battista, L. E. P. López, G. Batignani, E. Lorchat, A. Virga, S. Berciaud, T. Scopigno, *Proc. Natl. Acad. Sci. U.S.A.* **2022**, *119* e2119726119.

[46] W. Lin, P. Zhuang, H. Chou, Y. Gu, R. Roberts, W. Li, S. K. Banerjee, W. Cai, D. Akinwande, *Appl. Phys. Lett.* **2019**, *114* 113103.

[47] X. Liu, B. Mao, X. Yang, M. Taghinejad, M. Panmai, S. Lan, W. Cai, B. Li, J. Yan, *Laser Photonics Rev.* **2022**, *16* 2100737.

[48] B. Yang, E. Molina, J. Kim, D. Barroso, M. Lohmann, Y. Liu, Y. Xu, R. Wu, L. Bartels, K. Watanabe, T. Taniguchi, J. Shi, *Nano Lett.* **2018**, *18* 3580.

[49] H. Hong, C. Wu, Z. Zhao, Y. Zuo, J. Wang, C. Liu, J. Zhang, F. Wang, J. Feng, H. Shen, J. Yin, Y. Wu, Y. Zhao, K. Liu, P. Gao, S. Meng, S. Wu, Z. Sun, K. Liu, J. Xiong, *Nat. Photon.* **2021**, *15* 510.

[50] D. Schmitt, J. P. Bange, W. Bennecke, G. Meneghini, A. AlMutairi, M. Merboldt, J. Pöhls, K. Watanabe, T. Taniguchi, S. Steil, D. Steil, R. T. Weitz, S. Hofmann, S. Brem, G. S. M. Jansen, E. Malic, M. Stefan, M. Reutzel, *arXiv:2305.18908* **2023**.

[51] D. Schmitt, J. P. Bange, W. Bennecke, A. AlMutairi, G. Meneghini, K. Watanabe, T. Taniguchi, D. Steil, D. R. Luke, R. T. Weitz, S. Steil, G. S. M. Jansen, S. Brem, E. Malic, S. Hofmann, M. Reutzel, M. Stefan, *Nature* **2022**, *608* 499.

[52] S. Dong, S. Beaulieu, M. Selig, P. Rosenzweig, D. Christiansen, T. Pincelli, M. Dendzik, J. D. Ziegler, J. Maklar, R. P. Xian, A. Neef, A. Mohammed, A. Schulz, M. Stadler, M. Jetter, P. Michler, T. Taniguchi,

K. Watanabe, H. Takagi, U. Starke, A. Chernikov, M. Wolf, H. Nakamura, A. Knorr, L. Rettig, R. Ernstorfer, *Nat. Commun.* **2023**, *14* 5057.

[53] V. Kravtsov, R. Ulbricht, J. M. Atkin, M. B. Raschke, *Nat. Nanotechnol.* **2016**, *11* 459.

[54] V. Kravtsov, S. AlMutairi, R. Ulbricht, A. R. Kutayiah, A. Belyanin, M. B. Raschke, *Phys. Rev. Lett.* **2018**, *120* 203903.

[55] T. Jiang, V. Kravtsov, M. Tokman, A. Belyanin, M. B. Raschke, *Nat. Nanotechnol.* **2019**, *14* 838.

[56] W. Luo, B. G. Whetten, V. Kravtsov, A. Singh, Y. Yang, D. Huang, X. Cheng, J. Tao, A. Belyanin, M. B. Raschke, *Nano Lett.* **2023**, *23* 1767.

[57] M. Z. Bellus, Ph.D. thesis, Univ. of Kansas, **2018**.

[58] Y. Hwang, T. Kim, N. Shin, *ACS Appl. Nano Mater.* **2021**, *4* 12034.

[59] E. Lorchat, S. Azzini, T. Chervy, T. Taniguchi, K. Watanabe, T. W. Ebbesen, C. Genet, S. Berciaud, *ACS Photonics* **2018**, *5* 5047.

[60] E. Lorchat, L. E. P. López, C. Robert, D. Lagarde, G. Froehlicher, T. Taniguchi, K. Watanabe, X. Marie, S. Berciaud, *Nat. Nanotechnol.* **2020**, *15* 283.

[61] T. L. Purz, E. W. Martin, W. G. Holtzmann, P. Rivera, A. Alfrey, K. M. Bates, H. Deng, X. Xu, S. T. Cundiff, *J. Chem. Phys.* **2022**, *156* 214704.

[62] K. Połczyńska, S. Le Denmat, T. Taniguchi, K. Watanabe, M. Potemski, P. Kossacki, W. Pacuski, J. Kasprzak, *Nanoscale* **2023**.

[63] T. Jiang, D. Huang, J. Cheng, X. Fan, Z. Zhang, Y. Shan, Y. Yi, Y. Dai, L. Shi, K. Liu, C. Zeng, J. Zi, J. E. Sipe, Y.-R. Shen, W.-T. Liu, S. Wu, *Nat. Photon.* **2018**, *12* 430.

[64] D. Kozawa, A. Carvalho, I. Verzhbitskiy, F. Giustiniano, Y. Miyauchi, S. Mouri, A. Castro Neto, K. Matsuda, G. Eda, *Nano Lett.* **2016**, *16* 4087.

[65] X. Liu, J. Pei, Z. Hu, W. Zhao, S. Liu, M.-R. Amara, K. Watanabe, T. Taniguchi, H. Zhang, Q. Xiong, *Nano Lett.* **2020**, *20* 5359.

[66] D. Basko, G. La Rocca, F. Bassani, V. Agranovich, *Eur. Phys. J. B* **1999**, *8* 353.

[67] M. Danckwerts, L. Novotny, *Phys. Rev. Lett.* **2007**, *98* 026104.

[68] V. Kravtsov, S. Berweger, J. M. Atkin, M. B. Raschke, *Nano Lett.* **2014**, *14* 5270.

[69] M. A. May, T. Jiang, C. Du, K.-D. Park, X. Xu, A. Belyanin, M. B. Raschke, *Nano Lett.* **2020**, *21* 522.

[70] M. I. Stockman, *Phys. Rev. Lett.* **2004**, *93* 137404.

[71] M. Palummo, M. Bernardi, J. C. Grossman, *Nano Lett.* **2015**, *15* 2794.

[72] P. Rivera, J. R. Schaibley, A. M. Jones, J. S. Ross, S. Wu, G. Aivazian, P. Klement, K. Seyler, G. Clark, N. J. Ghimire, J. Yan, D. G. Mandrus, W. Yao, X. Xu, *Nat. Commun.* **2015**, *6* 6242.

[73] C. Jin, J. Kim, K. Wu, B. Chen, E. S. Barnard, J. Suh, Z. Shi, S. G. Drapcho, J. Wu, P. J. Schuck, S. Tongay, F. Wang, *Adv. Funct. Mater.* **2017**, *27* 1601741.

[74] S. Roy, A. S. Sharbirin, Y. Lee, W. B. Kim, T. S. Kim, K. Cho, K. Kang, H. S. Jung, J. Kim, *Nanomater.* **2020**, *10* 1032.

[75] N. B. Mohamed, F. Wang, H. E. Lim, W. Zhang, S. Koirala, S. Mouri, Y. Miyauchi, K. Matsuda, *Phys. Status Solidi (B)* **2017**, *254* 1600563.

[76] T. Forster, *Ann. Phys.* **1948**, *437* 55.

[77] J. He, T. Li, L. Zhang, D. He, Y. Wang, H. Ding, N. Pan, H. Zhao, *ACS Omega* **2018**, *3* 11930.

[78] D. L. Dexter, *J. Chem. Phys.* **1953**, *21* 836.

[79] J. A. Tomko, E. L. Runnerstrom, Y.-S. Wang, W. Chu, J. R. Nolen, D. H. Olson, K. P. Kelley, A. Cleri, J. Nordlander, J. D. Caldwell, O. V. Prezhdo, J.-P. Maria, P. E. Hopkins, *Nat. Nanotechnol.* **2021**, *16* 47.

[80] Y. Jiang, L. Miao, G. Jiang, Y. Chen, X. Qi, X.-f. Jiang, H. Zhang, S. Wen, *Sci. Rep.* **2015**, *5* 1.

[81] Y. Koo, H. Lee, T. Ivanova, A. Kefayati, V. Perebeinos, E. Khestanova, V. Kravtsov, K.-D. Park, *Light Sci. Appl.* **2023**, *12* 59.

[82] E. Liu, E. Barré, J. van Baren, M. Wilson, T. Taniguchi, K. Watanabe, Y.-T. Cui, N. M. Gabor, T. F. Heinz, Y.-C. Chang, C. H. Lui, *Nature* **2021**, *594* 46.

[83] C. Ropers, C. Neacsu, T. Elsaesser, M. Albrecht, M. Raschke, C. Lienau, *Nano Lett.* **2007**, *7* 2784.

[84] S. Berweger, J. M. Atkin, R. L. Olmon, M. B. Raschke, *J. Phys. Chem. Lett.* **2010**, *1* 3427.

[85] S. Berweger, J. M. Atkin, X. G. Xu, R. L. Olmon, M. B. Raschke, *Nano Lett.* **2011**, *11* 4309.

Table of Contents

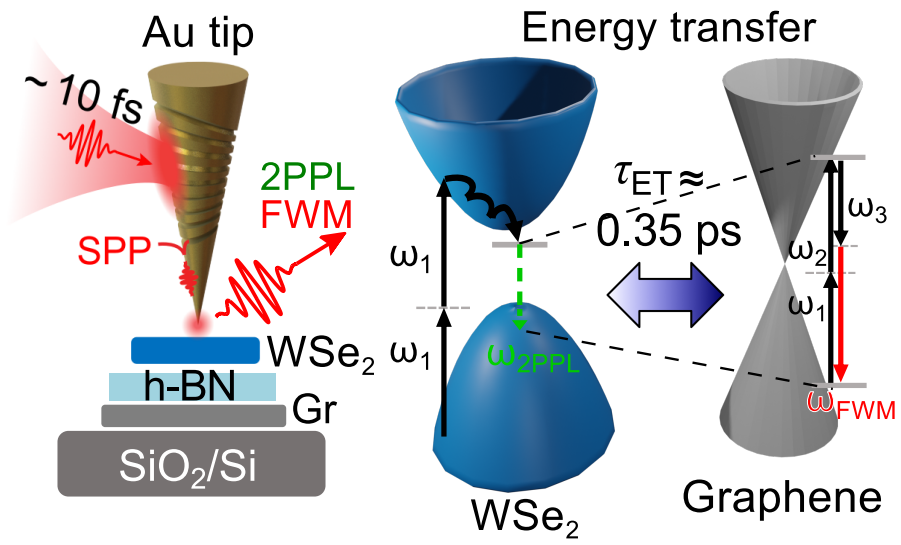

Resolving interlayer coupling in 2D heterostructures is difficult in general, especially in the presence of defects and disorder. We apply femtosecond nano-probe imaging combining coherent FWM and incoherent 2PPL to resolve the interlayer coupling in WSe_2 /graphene heterostructures. Using hBN spacer layers, we discover that energy transfer dominates the interlayer coupled response, with timescale of ∼0.35 ps.